Negative Thermal Expansion in ZrW_2O_8 and HfW_2O_8

J. S. O. Evans,† T. A. Mary,† T. Vogt,‡ M. A. Subramanian,§ and A. W. Sleight*,†

Department of Chemistry and Center for Advanced Materials Research, Oregon State University, Corvallis, Oregon 97331-4003; Physics Department, Brookhaven National Laboratory, Upton, New York 11973-5000; Experimental Station, The DuPont Company, Wilmington, Delaware 19880-0328

Received May 23, 1996. Revised Manuscript Received July 29, 1996⊗

Isostructural ZrW_2O_8 and HfW_2O_8 show strong negative thermal expansion from 0.3 K up to their decomposition temperatures of approximately 1050 K. This behavior is especially unusual because these compounds are apparently cubic over their entire existence range. Detailed structural studies of ZrW_2O_8 were conducted using high-resolution neutron powder diffraction data taken at 14 temperatures from 0.3 to 693 K. Below 428 K, ZrW_2O_8 adopts the acentric space group $P2_13$ and has a well-ordered structure containing corner-sharing ZrO_6 octahedra and two crystallographically distinct WO_4 tetrahedra. Above the phase transition at 428 K, which appears to be second order, the space group becomes centric $Pa\bar{3}$. The structure is now disordered with one oxygen site 50% occupied, suggesting the possibility of high oxygen mobility. Oxygen motion above 428 K is also suggested by dielectric and ac impedance measurements. The negative thermal expansion of ZrW_2O_8 and HfW_2O_8 is related to transverse thermal vibrations of bridging oxygen atoms. These lead to coupled rotations of the essentially rigid polyhedral building blocks of the structure. A semiquantitative model for both the negative thermal expansion and phase transition of these materials is proposed in light of the diffraction results.

Introduction

As temperature is increased, some increase in bond lengths is generally expected. The actual amount of expansion is related to the strength of the bond.[1,2] Thus, very strong bonds, such as those between oxygen and high-valent cations, typically show no detectable change in bond length over a temperature range as large as 1000 °C. On the basis of these considerations, very low thermal expansion might be expected for some materials, but negative thermal expansion cannot be anticipated based on the thermal expansion behavior of bonds. Nonetheless, negative thermal expansion does occasionally occur, and there seem to be several different mechanisms for its occurrence.

The average bond length of bonds within a polyhedron is expected to decrease as it becomes less distorted.[3] Frequently, distorted polyhedra become less distorted with increasing temperature. This increase in regularity can then lead to a decrease in average bond length and can be the reason for negative thermal expansion in, for example, perovskites with ferroelectric-type distortions of octahedra. In $BaTiO_3$ and $PbTiO_3$, negative thermal expansion close to their ferroelectric transitions[4,5] can be attributed to TiO_6 octahedra becoming more regular. In these cases, individual Ti−O distances show considerable lengthening or shortening with increasing temperature. In $BaTiO_3$, negative thermal expansion is limited to a few degrees very close to its phase transitions.[4] In $PbTiO_3$, negative thermal expansion occurs over a temperature range of nearly 500 °C.[5] However in both $BaTiO_3$ and $PbTiO_3$, negative thermal expansion occurs only when these materials are noncubic and when the thermal expansion is in fact highly anisotropic.

In some anisotropic materials, the normal thermal expansion of certain bonds causes thermal expansion in one or two dimensions, and this expansion rotates polyhedra in a way that results in contraction in other directions.[6] This mechanism can lead to very low volume thermal expansion in structures such as cordierite [$Mg_2Al_2Si_5O_{18}$] and NZP [$NaZr_2(PO_4)_3$]. This mechanism has never been proven to actually give a negative volume thermal expansion.

In some open structures with interstitial cations, the interstitial cations may alter their distribution over available sites with changing temperature, and this also can be a mechanism for negative thermal expansion. This mechanism has been proposed for the negative volume thermal expansion of β-eucryptite and may also apply to some members of the NZP family.[6]

Negative thermal expansion has been reported for three anisotropic materials in the Ta_2O_5−WO_3 system.[7] The most pronounced negative thermal expansion is observed in $Ta_{16}W_{18}O_{94}$ from room temperature to about 400 °C. No diffraction data as a function of temperature are available for this compound. Strong variations in thermal expansion behavior on thermal cycling suggest that some of the behavior is related to microstructure changes rather than to changes at the unit-cell level.

* To whom correspondence should be addressed.
† Oregon State University.
‡ Brookhaven National Laboratory.
§ The DuPont Co.
⊗ Abstract published in *Advance ACS Abstracts*, September 1, 1996.
(1) Megaw, H. D. *Z. Kristallogr.* **1938**, *A100*, 58.
(2) Hazen, R. M.; Prewitt, C. T. *Am. Miner.* **1977**, *62*, 309−315.
(3) Brown, I. D.; Shannon, R. D. *Acta Crystallogr.* **1973**, *A29*, 266.
(4) Shirane, G.; Takeda, A. *J. Phys. Soc. Jpn.* **1951**, *7*, 1.
(5) Shirane, G.; Hoshina, S. *J. Phys. Soc. Jpn.* **1951**, *6*, 265.
(6) Sleight, A. W. *Endeavour* **1995**, *19*, 64.
(7) Holcombe, C. E.; Smith, D. D. *J. Am. Ceram. Soc.* **1978**, *61*, 163.

S0897-4756(96)00295-5 CCC: $12.00

Another accepted mechanism for negative thermal expansion is transverse thermal motion.[8] This is the common explanation for the negative thermal expansion which Si and certain other materials with a Si-related structure show at low temperatures. Examples include GaP, InP, InSb, and AgI.[9−13] Such a mechanism is favored by a 2-coordinate anion or cation. A coordination number of two for a cation is rare; thus, it is not surprising that we have only one known example of negative thermal expansion in a metal oxide with a 2-coordinate cation, Cu_2O. The thermal expansion in Cu_2O is negative below room temperature but becomes positive above room temperature.[14]

Negative thermal expansion occurs in three crystalline forms of SiO_2 (quartz, cristobalite, and tridymite), but only at temperatures over 1000 °C.[15] This behavior is commonly attributed to the transverse thermal motion of oxygen in the Si−O−Si linkages. Several quartz and cristobalite derivative compounds (e.g., $AlPO_4$ and $FePO_4$) show negative thermal expansion at high temperatures, presumably due again to transverse thermal motion of oxygen.[16] Negative thermal expansion has also been observed in closely related zeolite structures.[17,18] In all these examples one can imagine transverse vibrations leading to a coupled rotation of coordination polyhedra within the materials. Evidence for such rotations has been obtained for β-cristobalite from the diffuse scattering in high-temperature electron diffraction patterns.[19] The negative thermal expansion of amorphous SiO_2 below room temperature has also been attributed to the transverse thermal motion of oxygen.[8]

The structures of cristobalite and Cu_2O are closely related, and it is therefore interesting to question why negative thermal expansion occurs only at low temperatures in Cu_2O and only at high temperatures in cristobalite. The ideal structures of these compounds are the same except that the cation and anion positions have been interchanged and the Cu_2O structure is twice as dense. The Cu_2O structure is actually two interpenetrating structures of the anticristobalite type. The consequence of this higher density is that the transverse thermal motion of copper becomes inhibited after it reaches a certain magnitude. It then begins interacting with the second interpenetrating network causing positive thermal expansion. There is no such interference of the transverse thermal motion of oxygen in the much more open cristobalite structure. However, in the ideal structure of cristobalite there is an instability of the 180° Si−O−Si bond angle and a static bending of this angle away from 180° when the temperature drops below approximately 200 °C (actual temperature depends highly on sample crystallinity and has been quoted in the range 120−272 °C). Even in β-cristobalite there remains controversy as to the exact nature of the high temperature form,[66] but once it has transformed into its low-temperature, more dense structure, it shows only positive thermal expansion.

Perhaps the most familiar example of a negative thermal expansion, though actually occurring at a phase transition, is that of ice. Both the normal hexagonal, I_h, and cubic, I_c, forms of ice have a density (0.92 g/cm^3) lower than liquid water; this property is crucial to the survival of aquatic life. In view of the structural relationship to the polymorphs of quartz (I_h being structurally related to trydimite, I_c to cristobalite) it is perhaps unsurprising that ice can also show negative thermal expansion in the solid state. Synchrotron studies show a negative thermal expansion for ice I_h below 73 K. Above this temperature positive thermal expansion is observed.[20]

Compounds with the cubic ZrP_2O_7 structure sometimes show negative thermal expansion above room temperature.[21−23] All oxygens are 2-coordinate in this structure. Thus, the negative thermal expansion is likely related to the transverse thermal motion of oxygen in the P−O−P and/or P−O−Zr linkages.

The ZrO_2−WO_3 pseudobinary phase diagram shows ZrW_2O_8 as the only ambient pressure phase. It is thermodynamically stable only over a narrow temperature range close to 1100 °C.[24] The structure of ZrW_2O_8 is related to that of ZrP_2O_7, and we have published a brief paper on its structure and its highly unusual negative thermal expansion.[25] The degree of thermal contraction is large and essentially constant over the temperature range 0.3−1050 K and is of a similar order of magnitude to the expansion observed for so called "high-expansion" normal ceramics [$\alpha \sim -9 \times 10^{-6}$ K^{-1} for ZrW_2O_8; $\alpha \geq +8 \times 10^{-6}$ K^{-1} for "high expansion" ceramics]. Isostructural HfW_2O_8 has essentially identical thermal expansion properties. These compounds thus find potential application both as pure phases with negative thermal expansion properties, and as components in composite materials with an overall zero bulk expansion. The room-temperature structure of ZrW_2O_8 was also reported independently by Auray et al.[26] In this paper, we give more details on the structure and characterization of this compound and isostructural HfW_2O_8. Structural results will be split into three sections: the low-temperature structure, the high-temperature structure, and the structural changes as a function of temperature. IR and dielectric measurements are also discussed. In light of these data, an overall model for the thermal expansion properties of this material is suggested and compared to experimental results.

(8) White, G. K. *Contem. Phys.* **1993**, *34*, 193.
(9) Blackman, M. *Philos. Mag.* **1958**, *9*, 831.
(10) Gibbons, D. F. *Phys. Rev.* **1958**, *112*, 136−140.
(11) Bienenstock, A.; Burley, G. *J. Phys. Chem. Sol.* **1963**, *24*, 1271−1278.
(12) Haruna, K.; Maeta, H.; Ohashi, K.; Koike, T. *J. Phys. C.: Solid State Phys.* **1986**, *19*, 5149−5154.
(13) Deus, P.; Schreider, H. A.; Voland, U.; Stiehler, K. *Phys. Solid State A* **1987**, *103*, 443.
(14) White, G. K. *J. Phys. C: Solid State Phys.* **1978**, *11*, 2171.
(15) Taylor, D. *Br. Ceram. Trans. J.* **1984**, *83*, 129.
(16) Taylor, D. *Br. Ceram. Trans. J.* **1986**, *85*, 147.
(17) Couves, J. W.; Jones, R. H.; Parker, S. C.; Tschaufeser, P.; Catlow, C. R. A. *J. Phys.: Condensed Matter* **1993**, *5*, L329−L332.
(18) Tschaufeser, P.; Parker, S. C. *J. Phys. Chem.* **1995**, *99*, 10600.
(19) Hua, G. L.; Welberry, T. R.; Withers, R. L.; Thompson, J. G. *J. Appl. Crystallogr.* **1988**, *21*, 458−465.
(20) Röttger, K.; Endriss, A.; Ihringer, J.; Doyle, S.; Kuhs, W. F. *Acta Crystallogr.* **1994**, *B50*, 644−648.
(21) Taylor, D. *Br. Ceram. Trans. J.* **1984**, *83*, 5.
(22) Korthuis, V.; Khosrovani, N.; Sleight, A. W.; Roberts, N.; Dupree, R.; Warren, W. W., Jr. *Chem. Mater.* **1995**, *7*, 412−417.
(23) Khosrovani, N.; Korthius, V.; Sleight, A. W. *Inorg. Chem.* **1996**, *35*, 485.
(24) Chang, L. L. Y.; Scroger, M. G.; Phillips, B. *J. Am. Ceram. Soc.* **1967**, *50*, 211−215.
(25) Mary, T. A.; Evans, J. S. O.; Sleight, A. W.; Vogt, T. *Science* **1996**, *272*, 90−92. Sleight, A. W.; Mary, T. A.; Evans, J. S. O. U.S. Patent No. 5,514,360, 1995.
(26) Auray, M.; Quarton, M.; Leblanc, M. *Acta Crystallogr.* **1995**, *C51*, 2210.

Experimental Details

The synthesis of ZrW_2O_8 has been described previously.[25] X-ray diffraction data for ZrW_2O_8 were collected using Cu Kα radiation with a Siemens D5000 diffractometer equipped with vertical Soller slits, computer-controlled antiscatter slits, and an energy-dispersive Kevex detector. Variable-temperature control was achieved using an in-house-designed resistively heated aluminum sample holder. Sample temperatures were read using a type K thermocouple situated next to the heater elements. High-temperature spectra were recorded with a step size of 0.02° 2θ and a step time of 0.5 s. Longer step times were used (7 s) for spectra used for detailed Rietveld analysis.

Neutron diffraction data were collected on the high-resolution powder diffractometer at beam line H1A of the high flux beam reactor (HFBR) at Brookhaven National Laboratory with a wavelength of 1.8857 Å. Fuller details of the experimental setup have been described elsewhere.[27,28] The multibank detector was moved in 0.02° (room temperature) or 0.05° (high/low temperature) steps, with integration times of 5 min/step. High-temperature spectra were recorded at 333, 373, 423, 483, 583, and 693 K using a furnace with resistive heating elements and an aluminum heat shield on a sample pressed into a cylindrical pellet 3 cm high and 1 cm in diameter. Two stainless steel coated thermocouples, one above and one below the sample, were used to monitor the temperature. Data collection did not commence until thermal equilibrium was achieved. Low-temperature spectra were recorded at 12, 20, 80, 150, and 220 K using a two-stage Air Products displex. The 3.3 K data set was recorded using a three-stage Air Products displex. Data at 0.3 K were recorded using a ^{4}He/^{3}He cryostat.

Accurate room-temperature cell parameters were obtained from laboratory X-ray data using an NBS Si 640b internal standard. Least-squares refinement of 2θ values of 61 independently indexed reflections out to $2\theta = 120°$, corrected for both sample displacement and zero-point shift, gave a cubic cell edge of 9.1575(2) Å. Because cell parameters and zero-points obtained from Rietveld refinement depend on the way in which peak profile (and in particular peak asymmetry) are modeled, cell parameters from neutron patterns were obtained via three separate protocols: (i) using an asymmetry corrected pseudo-Voigt peak shape within GSAS[29] [room temperature a = 9.15975(5) Å]; (ii) using a pseudo-Voigt function with no asymmetry [room temperature a = 9.15510(5) Å]; and (iii) using a least-squares fit to the positions of 20 high angle (2θ > 100°) reflection positions determined by Gaussian profile fitting [room temperature a = 9.1568(3) Å].[30,31] We emphasize that the esd of the cell parameter obtained by Rietveld analysis does not represent the true precision of cell parameter determination. Identical variations of the cell parameter with temperature were obtained by each method. Cell edges reported in Figure 1 and Table 1 are based on the last protocol. Bond distances and angles are based on cell dimensions obtained in the presence of an asymmetry correction.

Structural refinements were performed using both the GSAS and Rietan suites of programs.[29,32] Care was taken to adopt a consistent strategy throughout. For each of the refinements reported, in addition to the atomic variables detailed in the text, a total of 21 parameters were refined: 12 background terms, 6 profile variables, zero point, cell parameter, and scale factor. Several low-temperature spectra showed a weak broad feature at ca. 100° 2θ. The data region from 98.5° to 101° was therefore excluded from each low-temperature data set. High-temperature spectra contained a total of six reflections due to the Al of the furnace construction. Because the positions of these reflections show a temperature dependence markedly different from those of the sample material, an entirely consistent treatment of their contribution to the diffraction profile is not practicable (different sample peaks overlapping different furnace peaks at each temperature). To achieve a consistent refinement strategy, it was decided to exclude furnace peaks rather than model them as additional phases in the diffraction pattern. A constant 2θ range centered approximately on each Al reflection was therefore excluded at each temperature; this results in a constant number of data points for each refinement. For final refinements as a function of temperature, data were separated into two blocks: (i) 0.3−293 K data sets were refined simultaneously in one least-squares job and (ii) temperatures of 293−693 K in a separate job. The 300 K refinement was thus performed twice to ensure consistency between the two refinement blocks. Tabulations of parameters as a function of temperature for various refinement models were performed via automated searches of the output files. Space considerations preclude the detailed tabulation of refinement results as a function of temperature. Important bond distances and angles are therefore presented graphically. Full tables of fractional atomic coordinates and distances and angles as a function of temperature have been deposited and are available from the authors.

Distance least-squares refinement to predict idealized structures for various cell volumes was performed within the Crystals suite of programs.[33] Zr−O distances were restrained to a value of 2.108(15) Å, $W-O_{terminal}$ to 1.705(15) Å, and $W-O_{bridging}$ to 1.819(15) Å. Bond angles were restrained with an esd of 0.1°. Zirconium was fixed at the origin and the positions of other atoms refined so as to minimize differences between prescribed and calculated distances and angles. For each cell edge several different refinement protocols were performed to ensure a global minimum was reached. Perfectly regular octahedra were obtained out to a cell edge of 9.2 Å. At 9.3 Å, distortions of 0.003 Å in bond lengths were required; by 9.4 Å these distortions reached 0.03 Å.

A Netzsch thermal analysis system was used to obtain DSC and dilatometer data. Fused silica was used for the internal components of the dilatometer. A sapphire standard was used for calibration purposes.

Dielectric constant and loss tangent measurements were performed in the frequency range 10^2-10^7 Hz using Hewlett-Packard (4284A and 4285A) LCR bridges. The samples were in the form of sintered pellets with sputtered gold as electrodes, and the data were corrected for porosity. Electrical conductivity measurements were done in air using a Hewlett-Packard (9213A) complex impedance analyzer. Measurement details are described elsewhere.[34]

IR spectra were recorded using KBr pellets on a Bruker IFS 66V FT-IR spectrometer with 64 scans and a resolution of 1 cm^{-1}. Raman spectra were recorded on a DILOR Z24 single-channel Raman spectrometer using an argon ion laser with 488 nm exciting line and 300 mW power. Temperature was measured by a copper−constantan thermocouple and is considered accurate to ±1 K.

The refractive index of ZrW_2O_8 was determined to be 1.669 by immersion methods.

Negative Thermal Expansion Properties

The negative thermal expansion properties of ZrW_2O_8 are shown in Figure 1. Figure 1a shows the temperature dependence of the cubic unit-cell edge from 0.3 to 693 K. An approximately linear decrease in cell dimension is seen over the entire temperature range. Figure

(27) Vogt, T.; Passell, L.; Cheung, S.; Axe, J. D. *Nucl. Instrum. Methods* **1993**, *A338*, 71−77.
(28) Axe, J. D.; Cheung, S.; Cox, D. E.; Passell, L.; Vogt, T. *J. Neutron Res.* **1994**, *2*, 85−95.
(29) (a) Larson, A. C.; Von Dreele, R. B. *LANSCE*, Los Alamos National Lab, Los Alamos, NM, 1994. (b) Howard, C. J. *J. Appl. Crystallogr.* **1982**, *15*, 615. (c) Le Bail, A. C.; Duroy, H.; Fourquet, J. L. *Mater. Res. Bull.* **1988**, *23*, 447.
(30) Brown, A.; Edmonds, J. W. *Adv. X-Ray Anal.* **1980**, *23*, 361.
(31) Cockroft, J. K. *Refcel* software.
(32) Izumi, F. In *The Rietveld Method*; Young, R. A., Ed.; OUP, UK, 1993; p 298.
(33) Watkin, D. J.; Carruthers, J. R.; Betteridge, P. W. *Crystals User Guide*; Chemical Crystallography Laboratory, University of Oxford, Oxford, 1985.
(34) Subramanian, M. A.; Rudolf, P. R.; Clearfield, A. *J. Solid State Chem.* **1985**, *60*, 172.

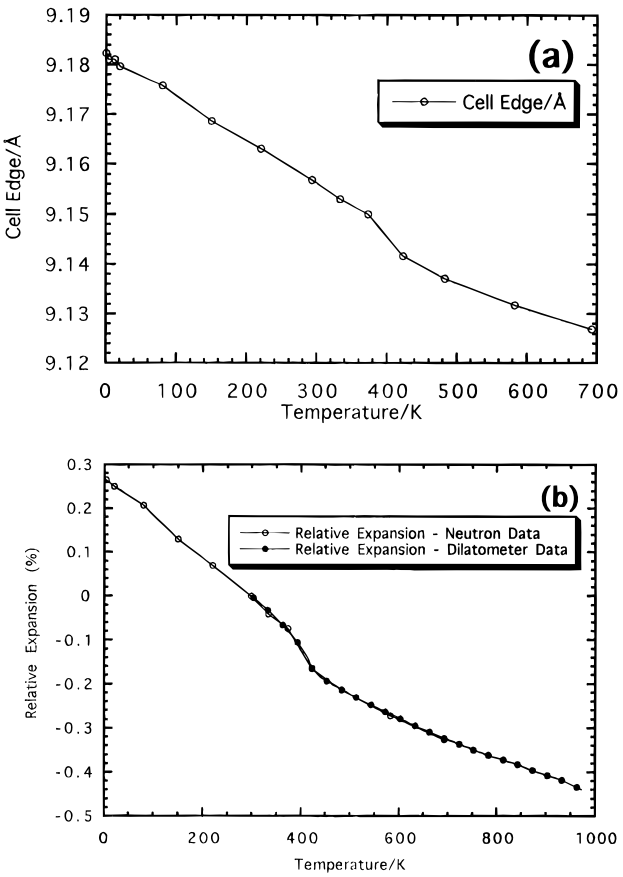

Figure 1. (a) Cubic cell dimension as a function of temperature. (b) Relative expansion from both diffraction and dilatometer data.

1b shows the percentage relative expansion [defined as $(l_T - l_{293}/l_{293}) \times 100$, where l_T is the length at a given temperature] from both diffraction (0.3−693 K) and dilatometer (293−1050 K) data. From the diffraction data we calculate an overall coefficient of thermal expansion [defined as $(l_{T2} - l_{T1})/(l_{T1} \times (T2 - T1))$] of $\alpha = -8.7 \times 10^{-6}$ K^{-1} between 0.3 and 693 K. Dilatometer measurements on sintered pressed pellets were consistent with this value within ±10%. A discontinuity in the dilatometer data is apparent around 430 K. From α versus T curves (i.e., derivatives of Figure 1b) we estimate a transition temperature of 428 K (defined as the minimum of the α vs T plot). The phase change responsible for this discontinuity is discussed in more detail below.

We note that the value of α of -8.7×10^{-6} K^{-1} represents a significant decrease in volume. Traditionally, thermal expansions of ceramics have been categorized into three broad groups: very low expansion [$0 \leq \alpha \leq +2 \times 10^{-6}$ K^{-1}], low expansion [$+2 \leq \alpha \leq +8 \times 10^{-6}$ K^{-1}], and high expansion [$\alpha \geq +8 \times 10^{-6}$ K^{-1}].[35]

Dielectric Behavior and Ionic Conductivity of ZrW_2O_8

The results of dielectric measurements on ZrW_2O_8 are given in Figure 2. The measured dielectric constant was relatively low (∼10) and showed a nearly frequency-independent behavior at room temperature, which is typical for an insulating dielectric ceramic. However, dielectric loss measurements at room temperature showed a small but systematic increase with decrease in frequency of the measurement. A plot of loss vs frequency (both on a logarithmic scale) showed a linear behavior without any dispersion at lower frequencies (Figure 2b). Both dielectric constant and loss showed similar trends in the range room temperature to 428 K. However, when the temperature of the measurement was raised above 428 K, *both* dielectric constant and loss clearly showed a marked frequency dependence, with the onset of a very strong dispersion at lower frequencies.

The observed dielectric constant and loss behavior can be rationalized as follows. Dielectric loss in ionic solids results from three primary effects: (1) ion migration losses (dc conductivity), (2) ion vibration and deformation losses, and (3) electron polarization losses. Of these, the most important process is ionic migration loss, which tends to show a large increase in the loss at low frequencies and a strong temperature dependence.[36] The nearly frequency-independent dielectric constant behavior observed at room temperature in ZrW_2O_8 indicates that the small but systematic increase in the dielectric loss with decreasing frequency is due to the latter two of the three effects mentioned above. The fact that the room-temperature dielectric loss is small (10^{-3}−10^{-2}) in the low-frequency region indicates that the loss behavior is most likely due to the very low concentration of localized or trapped electronic charge carriers (especially at grain boundaries), which is common among insulating oxides containing transition metal cations. The dielectric behavior of ZrW_2O_8 observed above 428 K (Figure 2c) is due to the onset of ionic displacements in the lattice. Both dielectric constant and loss show a clear temperature dependence with a strong dispersion at low frequencies. Such a behavior is observed in many ionic conductors containing mobile ionic charge carriers, for example, $K_xAl_xTi_{8-x}O_{16}$.[37] Indeed, the complex impedance measurements strongly suggest that ZrW_2O_8 exhibits appreciable ionic conductivity above 428 K. The magnitude of ionic conductivity above the phase transition of $\sigma \sim 10^{-5}$ Ω^{-1} cm^{-1} compares to a value of ca. 10^{-4} Ω^{-1} cm^{-1} for cubic stabilized zirconia at 700 K.[38] A plot of log σ vs $1/T$ (Figure 2d) showed a linear behavior with an activation energy of 0.5 eV. At room temperature, ZrW_2O_8 acts as an insulator with conductivities in the range $\leq 10^{-8}$ Ω^{-1} cm^{-1}.

Room-Temperature Structure of ZrW_2O_8

Initial examination of the powder neutron and X-ray diffraction patterns of ZrW_2O_8 revealed that all peaks could be indexed on a cubic cell, $a = 9.1575$ (2) Å. This compares with previously reported cell edges of 9.154,[39] 9.159,[24] 9.08,[40] 9.123,[41] and 9.1456 Å.[26] The observed systematic absences ($h00$: $h = 2n$) suggested space

(35) Roy, R.; Agrawal, D. K.; McKinstry, H. A. *Annu. Rev. Mater. Sci.* **1989**, *19*, 59−81.
(36) Jonscher, A. *Dielectric Relaxation in Solids*; Chelsea Dielectric Press: London, 1983.
(37) Jonscher, A. K.; Deori, K. L.; Reau, J.-M.; Moali, J. *J. Mater. Sci.* **1979**, *14*, 1308.
(38) Kilner, J. A. In The Encyclopaedia of Advanced Materials; Bloor, D., Brock, R. J., Flemings, M. C., Mahajan, S., Cahn, R. W., Eds.; Pergamon: New York, 1994; p 787.
(39) Graham, J. D.; Wadsley, A. D.; Weymouth, J. H.; Williams, L. S. *J. Am. Ceram. Soc.* **1959**, *42*, 570.
(40) Thoret, J. *Rev. Chim. Miner.* **1974**, *11*, 237−261.
(41) Palytsyna, S. S.; Mokhosoev, M. V.; Krivobok, V. I. *Bull. Acad. Sci. USSR Div. Chem. Sci.* **1977**, *26*, 611−613.

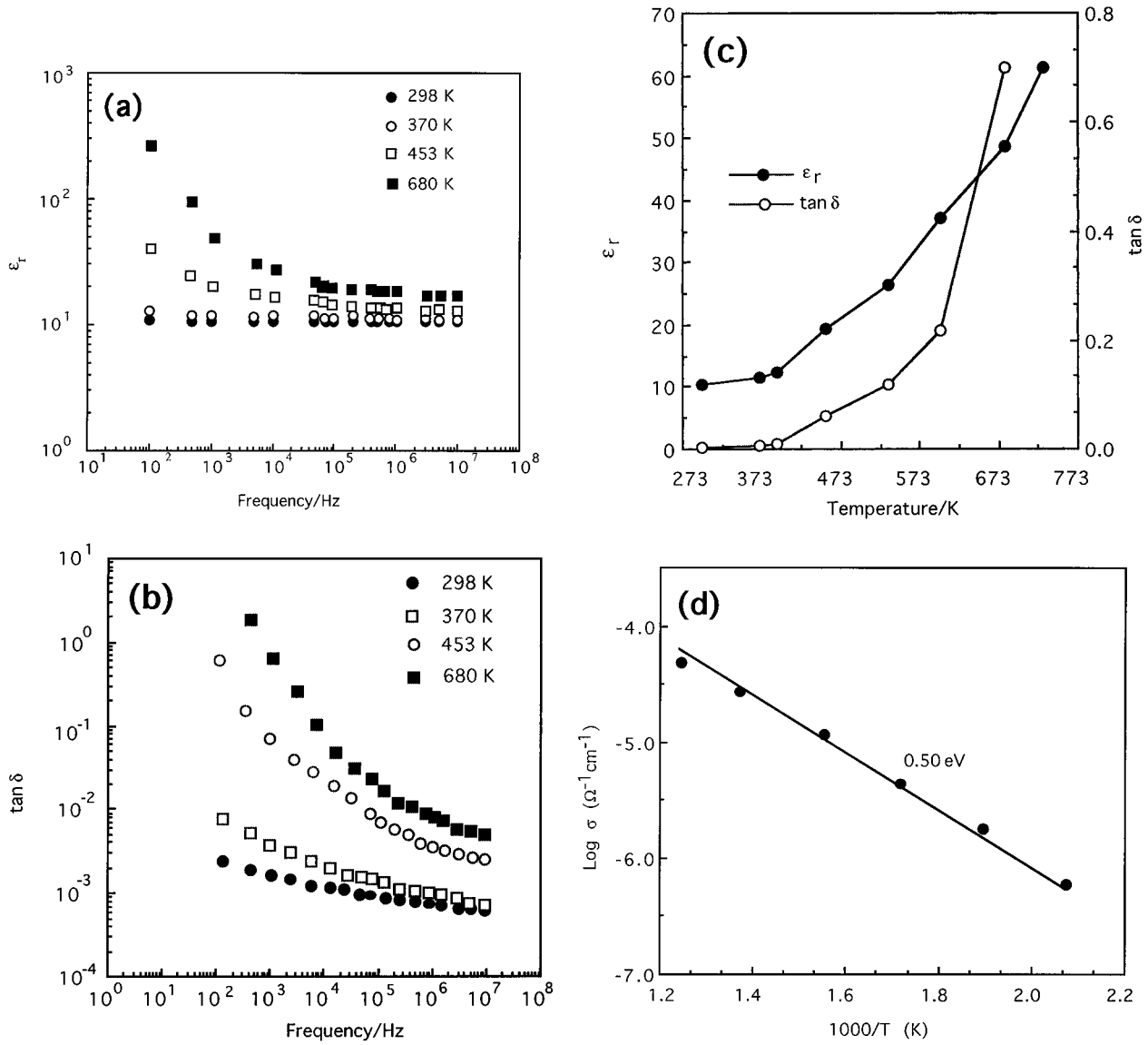

Figure 2. (a) Variation of relative dielectric constant (ϵ_r) versus measurement frequency (Hz). (b) Variation of dielectric loss (tan δ) with measurement frequency (Hz). Note that data in (a) and (b) are plotted on a logarithmic scale. (c) Low-frequency dielectric constant (ϵ_r) and loss (tan δ) as a function of temperature. A marked increase in both ϵ_r and tan δ is observed above 428 K. (d) Arrhenius plot of log conductivity versus reciprocal temperature for ZrW_2O_8.

groups $P2_13$ (No. 198) or $P4_232$ (No. 208). Similarities to ZrV_2O_7 prompted adoption of the former space group. Integrated intensities were extracted from both the X-ray and neutron diffraction patterns using the Le Bail method.[29] These intensity data were then used in the direct methods package Sirpow-92,[42] to obtain possible atomic positions; no distinction could, however, be made between Zr, W, and O atoms. Patterson synthesis of the X-ray data was therefore used in conjunction with the direct methods data to identify Zr−W and W−W vectors. The resulting trial set of metal positions was refined using the X-ray data. These refined positions were then used in conjunction with the neutron data to calculate a difference Fourier map. Potential oxygen sites were identified by this method; those which seemed reasonable in light of the Patterson functions and direct methods results were included in subsequent cycles of least-squares refinement. In this manner it proved possible to develop a chemically sensible structural model which showed excellent agreement with both X-ray and neutron diffraction data.

During final cycles of least-squares refinement, the usual profile (6 variables), background (12 variables), scale factor, and cell parameter were refined along with fractional coordinates (11 variables), and either isotropic (7 variables) or anisotropic (22 variables) thermal parameters for each atom. For an isotropic refinement this corresponds to a ratio of approximately nine expected reflections per structural parameter. Final agreement factors: Isotropic: wR_p = 10.44%, R_p = 7.92%, $R(F^2)$ = 6.50%, χ^2 = 1.0; Anisotropic: wR_p = 9.66%, R_p = 7.10%, $R(F^2)$ = 3.07%, χ^2 = 0.9 (no excluded regions, 6749 data points) were obtained. Final observed, calculated and difference plots are shown in Figure 3; details of the refinement in Table 1; fractional atomic coordinates are given in Table 2a, and selected bond distances are shown graphically in Figure 10. Clearly the use of anisotropic thermal parameters is questionable given the low number of observations. This

(42) Altomare, A.; Cascarano, G.; Giacovazzo, C.; Guagliardi, A.; Burla, M. C.; Polidori, G.; Camalli, M. *J. Appl. Crystallogr.* **1994**, *27*, 435.

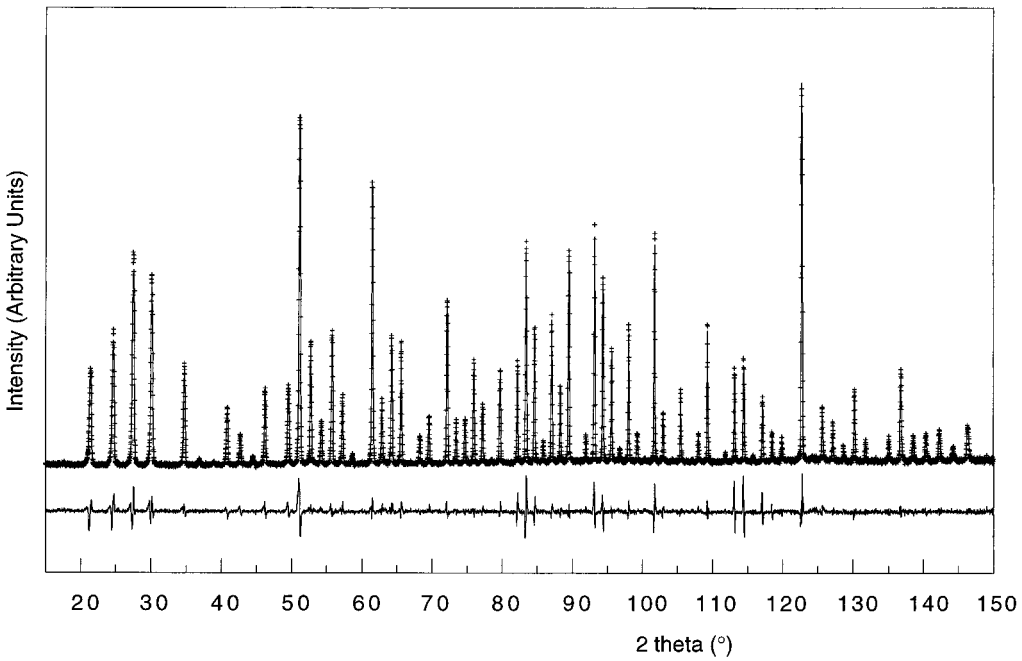

Figure 3. Observed (+), calculated (—), and difference (lower plot) room-temperature neutron diffraction patterns.

Table 1. Refinement Details

			isotropic model		anisotropic model				rigid-body model	
temperature (K)	cell parameter (Å)[a]	space group	wRp (%)	params[b]	wRp (%)	R(F^2)	χ^2 [c]	params	wRp (%)	params
0.3	9.1823(4)	$P2_13$	11.05	18	10.87	5.07	3.1	33	11.04	12
3.3	9.1810(5)	$P2_13$	13.34	18	13.25	4.98	7.3	33	13.38	12
12	9.1810(5)	$P2_13$	12.13	18	12.03	4.86	5.9	33	12.12	12
20	9.1797(6)	$P2_13$	13.36	18	13.23	5.12	6.1	33	13.37	12
80	9.1758(5)	$P2_13$	10.87	18	10.70	4.59	4.1	33	10.86	12
150	9.1686(5)	$P2_13$	12.04	18	11.80	6.00	5.1	33	11.97	12
220	9.1631(5)	$P2_13$	10.88	18	10.64	5.57	4.8	33	10.79	12
293[d]	9.1568(3)	$P2_13$	10.47	18	9.69	3.12	0.88	33	10.05	12
333	9.1530(3)	$P2_13$	7.55	18	6.82	6.23	0.85	33	7.22	12
373	9.1500(4)	$P2_13$	7.50	18	6.73	6.35	0.82	33	7.19	12
423[e]	9.1416(5)				9.97	8.61	0.99	33		
483	9.1371(5)	$Pa\bar{3}$	7.32	11	5.93	5.77	0.64	19	6.36	9
583	9.1318(4)	$Pa\bar{3}$	7.34	11	5.69	5.85	0.59	19	6.17	9
693	9.1269(4)	$Pa\bar{3}$	7.35	11	5.51	7.01	0.57	19	6.04	9

[a] Cell parameter based on refinement of high-angle peaks fitted with pseudo-Voigt function. [b] Number of parameters quoted is number of structural parameters. An additional 21 "histogram" parameters were refined for each phase (see text). [c] High background due to the furnace at temperatures above 293 K leads to artificially low values of wR_p, and χ^2 values lower than 1 (see text). [d] 293 K refinements performed with both low- and high-temperature protocols. Values of wR_p differed by <0.02%. Values quoted are for low-temperature protocol. [e] Neither structural model gave a good agreement to 423 K data set (see text). Values quoted are for a single W site refinement in $P2_13$.

point is considered in more detail below, as are rigid-body models of refinement which help reduce the number of free variables. We emphasize, however, that each model led to similar trends in bond distances and angles as a function of temperature. This structural model also gave excellent agreement with the X-ray data, final agreement factors of $wR_p = 9.8\%$, $R_p = 7.0\%$, $R(F^2) = 7.3\%$ and $\chi^2 = 1.0$ (10—150°, 7001 data points) being obtained. The maximum shift of metal atom positions from those of Table 2 was 0.01 Å. A section of the observed and calculated X-ray spectrum is included in Figure 6.

Discussion of the Room-Temperature Structure

A view of the room-temperature ZrW_2O_8 structure showing thermal ellipsoids is given in Figure 4a, and a polyhedral representation in Figure 4b. The structure is comprised of corner-sharing WO_4 tetrahedra and ZrO_6 octahedra linked such that each octahedron shares corners with six separate WO_4 tetrahedra, but each WO_4 tetrahedron shares only three of its four oxygens with adjacent octahedra. This results in one oxygen per tetrahedron that is bonded solely to W (for O4 the next nearest adjacent metal being some 3.6 Å distant). The terminal W—O bond distances are significantly shorter than those that are involved in a W—O—Zr linkage, 1.705 vs 1.801 Å for W1 and 1.731 vs 1.783 Å for W2. The longer W—O distances are more typical of those normally found in WO_4 tetrahedra.

The existence of terminal M—O bonds in the solid state is well established for octahedrally coordinated W(VI) and Mo(VI) as well as for pseudooctahedral V(V) in compounds such as V_2O_5.[43] Whereas stoichiometrically analogous $ZrMo_2O_8$ and $HfMo_2O_8$ form trigonal-layered structures which are not directly related to that of ZrW_2O_8, the MoO_4 units also feature a terminal

(43) Pope, M. T.; *Heteropoly & Isopoly Oxometalates*; Springer-Verlag: New York, 1983.

Table 2

atom	occupancy	*x/a*	*y/b*	*z/c*	U_{eq}/Å^2 [a]
(a) Fractional Atomic Coordinates at 293 K, Anisotropic Refinement Model, $P2_13$					
Zr1	1.0	0.0004(3)	0.0004(3)	0.0004(3)	0.008
W1	1.0	0.3409(3)	0.3409(3)	0.3409(3)	0.010
W2	1.0	0.6009(3)	0.6009(3)	0.6009(3)	0.006
O1	1.0	0.0529(3)	−0.2069(3)	−0.0619(4)	0.020
O2	1.0	0.0697(4)	−0.0575(3)	0.2132(3)	0.017
O3	1.0	0.4941(4)	0.4941(4)	0.4941(4)	0.022
O4	1.0	0.2322(3)	0.2322(3)	0.2322(3)	0.035
(b) Fractional Atomic Coordinates at 483 K, Anisotropic Refinement Model, $Pa\bar{3}$					
Zr1	1.0	0.0000(0)	0.0000(0)	0.0000(0)	0.014
W1	0.5	0.3394(5)	0.3394(5)	0.3394(5)	0.011
W2	0.5	0.6035(5)	0.6035(5)	0.6035(5)	0.011
O1	1.0	0.0549(3)	−0.2089(2)	−0.0671(3)	0.036
O3[b]	0.5	0.5055(0)	0.5055(0)	0.5055(0)	0.044
O4	0.5	0.2322(4)	0.2322(4)	0.2322(4)	0.064

[a] Defined as one-third of the trace of the diagonalized matrix. [b] Due to its proximity to the center of inversion at (0.5, 0.5, 0.5), the position of O3 was found to fluctuate at 0.5 ± 0.055 and was therefore fixed during final cycles of refinement.

oxygen atom.[44−46] To our knowledge, this is the first structurally characterized example of a terminal oxygen in a tetrahedral WO_4 unit. This low oxygen coordination is perhaps one of the main reasons why ZrW_2O_8 is thermodynamically stable over only a narrow temperature region.

The structural relationship between ZrW_2O_8 and the previously reported cubic pyrophosphates and vanadates AM_2O_7 [A = Zr, Hf, Sn, U, etc.; M = V, P, As] is shown schematically in Figure 5. Both structures contain AO_6 octahedra and MO_4 tetrahedra linked by shared corners only. In ZrV_2O_7 there is a single "bridging" oxygen which completes the tetrahedral coordination of each V forming a pyrovanadate group. The presence of the eighth oxygen in ZrW_2O_8 can be conceptually thought of as "splitting" the $M_2O_7^{4-}$ unit into two separate WO_4^{2-} tetrahedral units. Thus each WO_4 unit contains one short $W-O_{terminal}$ bond (1.7 Å) with a significantly longer (2.4 Å) distance between the terminal oxygen of one tetrahedron and the W of the adjacent tetrahedron. This longer distance is too long to be considered as a normal W−O bonding distance (octahedral bond distances in monoclinic WO_3 vary from 1.73 to 2.18.[47] That there is, however, some interaction between W1 and the "terminal" O of the adjacent WO_4 group is revealed by the small distortions in bond angles around W1 from ideal tetrahedral values. The O−W−O bond angles are 101.7° and 116.0° for W1 as compared to 109.1° and 109.8° for W2. These distortions could also be due to the relatively short O3−O1 distance of 2.688 Å. Valence calculations[48,49] show that the W1−O3 "nonbonding" interaction contributes approximately 5% of the total valence sum of W1 and 15% of O3. Further evidence of interaction between these two

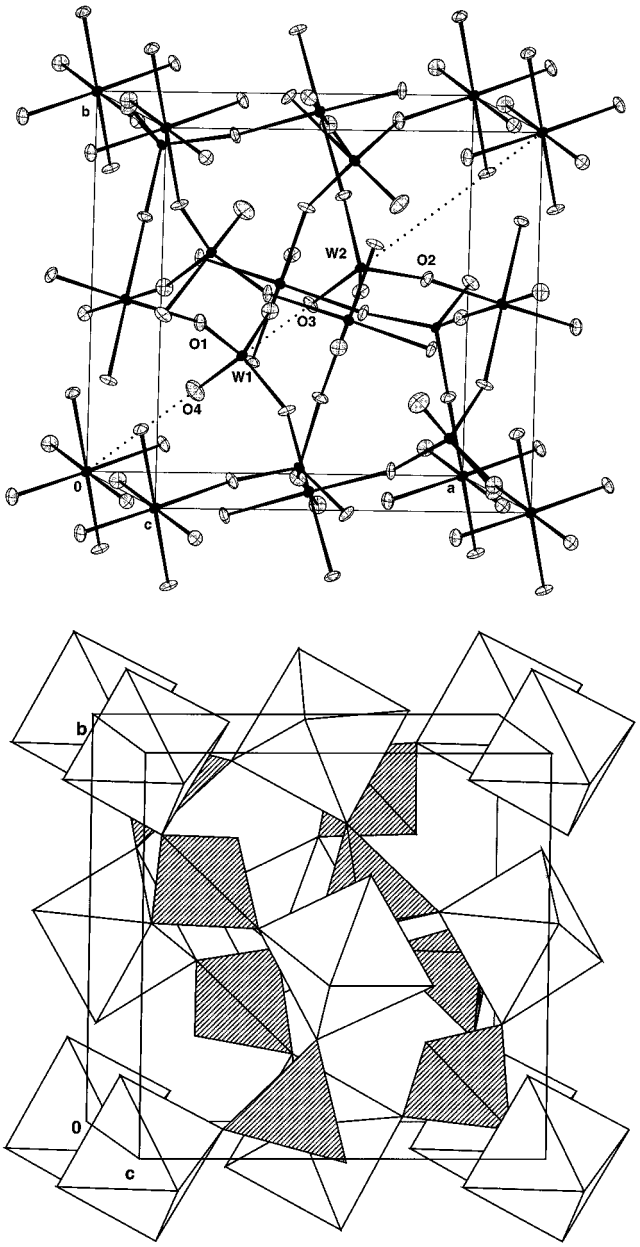

Figure 4. (a) Unit cell of ZrW_2O_8, with 90% thermal ellipsoids drawn. (b) Polyhedral representation of the structure. ZrO_6 octahedra shown in white, WO_4 tetrahedra shaded.

atoms comes from the somewhat unusual thermal parameters of O3 (vide infra). The lack of strong bridging W−O−W bonds is associated with the lack of an inversion center at O3 (approximate coordinates: $^1/_2,^1/_2,^1/_2$), which is present in the cubic AM_2O_7 structures. The inversion center present in cubic AM_2O_7 phases with space group $Pa\bar{3}$ is destroyed in room-temperature ZrW_2O_8, primarily by the presence of the eighth oxygen (O4) and resultant shifts of W atoms. Lacking the inversion center, the space group becomes $P2_13$.

High-Temperature Structure

X-ray and neutron diffraction give clear evidence for the phase transition observed at 428 K by dilatometry. Figure 6 shows X-ray patterns recorded at three representative temperatures. The spectral changes observed and, in particular, the disappearance of the (310) reflection ($h \neq 2n$), indicate the adoption of the centrosymmetric space group $Pa\bar{3}$ (No. 205). Although

(44) Auray, M.; Quarton, M.; Tarte, P. *Powder Diffraction* **1987**, *2*, 36−38.
(45) Auray, M.; Quarton, M.; Tarte, P. *Acta Crystallogr.* **1986**, *C42*, 257−259.
(46) Serechkin, V. N.; Efrenov, V. A.; Trunov, V. K.; *Russ. J. Inorg. Chem.* **1987**, *32*, 1568−1570.
(47) Woodward, P.; Sleight, A. W.; Vogt, T. *J. Phys. Chem. Solids* **1995**, *56*, 1305.
(48) Brown, I. D.; Altermatt, D. *Acta Crystallogr.* **1985**, *B41*, 244−247.
(49) Brese, N. E.; O'Keefe, M. *Acta Crystallogr.* **1991**, *B47*, 192−197.

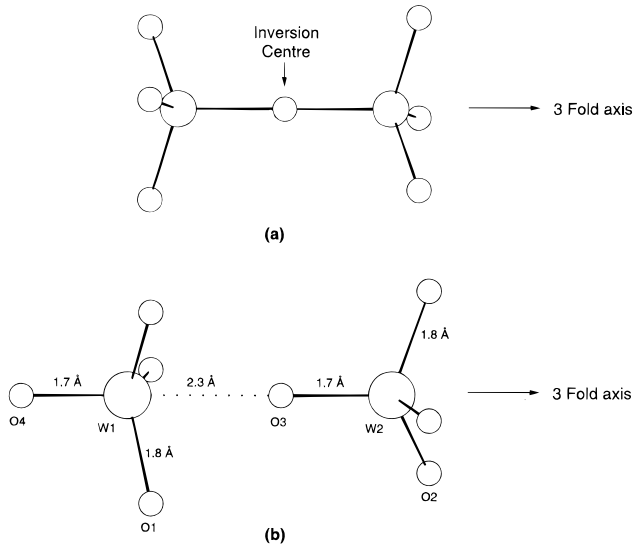

Figure 5. Relationship between the $M_2O_7^{4-}$ unit of ZrP_2O_7 and ZrV_2O_7 and the tetrahedral units of ZrW_2O_8.

initial refinement suggested that reasonable agreement [$\chi^2 = 0.94$, $wR_p = 6.9\%$, $R_F = 7.4\%$] to the observed data could be obtained using a model containing a single W site, analysis of "thermal" parameters revealed considerable disorder (corresponding to root-mean-square atomic displacements >0.5 Å) of the tungsten atom along the 3-fold axis.

Successful refinement of both the X-ray and neutron diffraction data could, however, be obtained using a model containing disordered W and O sites on the 3-fold axis. Using the atomic positions of Table 2b, an excellent fit to the observed data could be obtained using either isotropic or anisotropic thermal parameters, with all atoms showing chemically sensible thermal parameters (Table 2b). The maximum atomic displacement between isotropic and anisotropic models being less than 1.5 esd's. Good agreement with the X-ray data was also obtained. The maximum atomic shift between the 483 K neutron and 509 K X-ray data being 0.02(1) Å. Observed and calculated X-ray profiles are included in Figure 6.

Figure 7 shows a schematic view of the threefold axis of the disordered model. The overall disordered atomic arrangement can be considered as the superposition of two ordered arrangements of WO_4 groups, related to those of the low temperature structure by inversion through ($^1/_2$,$^1/_2$,$^1/_2$). The data are therefore consistent with a model containing a 50% time average of two discrete orientations of WO_4 tetrahedra. On such a basis, individual W−O bond lengths within the tetrahedra consistent with those at low temperature are obtained (Figure 10). To check the validity of such a model, and in particular the implied two-site disorder of terminal oxygens, refinements were also performed in the noncentrosymmetric subgroup $P2_13$. Despite the expected correlations between related atoms, the model remained ultimately stable to refinement; no evidence for preferential occupancy of either oxygen site was found.

This structure then suggests that ZrW_2O_8 undergoes a highly unusual order−disorder transition on heating. The success of the positionally disordered model in fitting experimental data suggests that the terminal oxygen, O4, is mobile at elevated temperatures. Migration of O4 from its original site at ca. (0.23, 0.23, 0.23) [i.e., 1.7 Å from W1] to a vacant site at (0.77, 0.23, 0.23) [i.e., 1.7 Å from W2] is likely to be the source of this disorder. This migration would then be accompanied by the relatively facile (~0.15 Å) migration of O3 from W2 to the adjacent W1, and the concerted migration of W1's original terminal oxygen. The process is shown schematically in Figure 8. Such a model could imply either long-range O^{2-} migration or relatively short-range O^{2-} hopping between adjacent WO_4 pairs of the type

$$4WO_4^{2-} \xrightarrow{T_c} W_2O_7^{2-} + W_2O_9^{6-} \Leftrightarrow W_2O_9^{6-} + W_2O_7^{2-}$$

Even if the instantaneous concentration of $W_2O_9^{6-}$ and $W_2O_7^{2-}$ is very small, their fleeting occurrence may be essential to disorder the orientations of the tetrahedra. Evidence for the high oxygen mobility implied by such a model comes from the dielectric and conductivity data of Figure 2.

One would also expect a marked change in vibrational spectra to accompany the structural change. Infrared spectra of ZrW_2O_8 recorded at six temperatures between 298 and 473 K are shown in Figure 9a, and spectral assignments suggested in Table 3. By comparison to spectra of other tungstates,[50−53] we assign the main bands centered at 999, 907, and 871 cm^{-1} to symmetric stretching of the WO_4 tetrahedra; those at 800, 760, 739, and 646 cm^{-1} to asymmetric stretches; and the broad structured band between 600 and 400 cm^{-1} to WO_4 asymmetric bending modes and ZrO_6 stretching modes. The band at 999 cm^{-1} we assign to terminal W═O stretching by analogy with reported stretching frequencies for octahedral tungstates containing one short W═O bond. The observed stretching frequency correlates well with the empirical relationship between W−O bond length and stretching frequency reported by Daniel.[54,55] Room-temperature data for HfW_2O_8 support our assignment.

As the material is warmed above 373 K, two new distinct bands appear at 668 and 419 cm^{-1}, whose intensity grows with increasing temperature. These modes are thus clearly related to the structural phase transition, and we assign them to vibrational modes occurring during the disordering process. Further work would be required to unambiguously determine whether these modes are due to stretching frequencies of distinct groups such as W_2O_9. We note, however, the assignment of W−O−W stretching and bending frequencies to bands around ca. 750 and 350 cm^{-1} in potassium lanthanide tungstates. In addition there is an apparent reduction in intensity of some bands assigned to WO_4 asymmetric stretches as the temperature is increased.

Variable-temperature Raman spectra are shown in Figure 9b,c. In contrast to the IR data, no dramatic changes are seen as a function of temperature, suggesting that the vibrational modes due to the disordering process observed by IR are Raman inactive. There is,

(50) Hanuza, J.; Macalik, L. *Spectrochim. Acta* **1987**, *43A*, 361.
(51) Hanuza, J.; Maczka, M. *Vibr. Spectrosc.* **1994**, *7*, 85.
(52) Tarte, P.; Liegeois-Duyckaerts, M. *Spectrochim. Acta* **1972**, *28A*, 2029.
(53) Liegeois-Duyckaerts, M.; Tarte, P. *Spectrochim. Acta* **1972**, *28A*, 2037.
(54) Daniel, M. F.; Desbat, B.; Lassegues, J. C.; Gerand, B.; Figlarz, M. *J. Solid State Chem.* **1987**, *67*, 235.
(55) Baran, E. J.; Botto, I. L.; Kinomura, N.; Kumada, N. *J. Solid State Chem.* **1990**, *89*, 144.

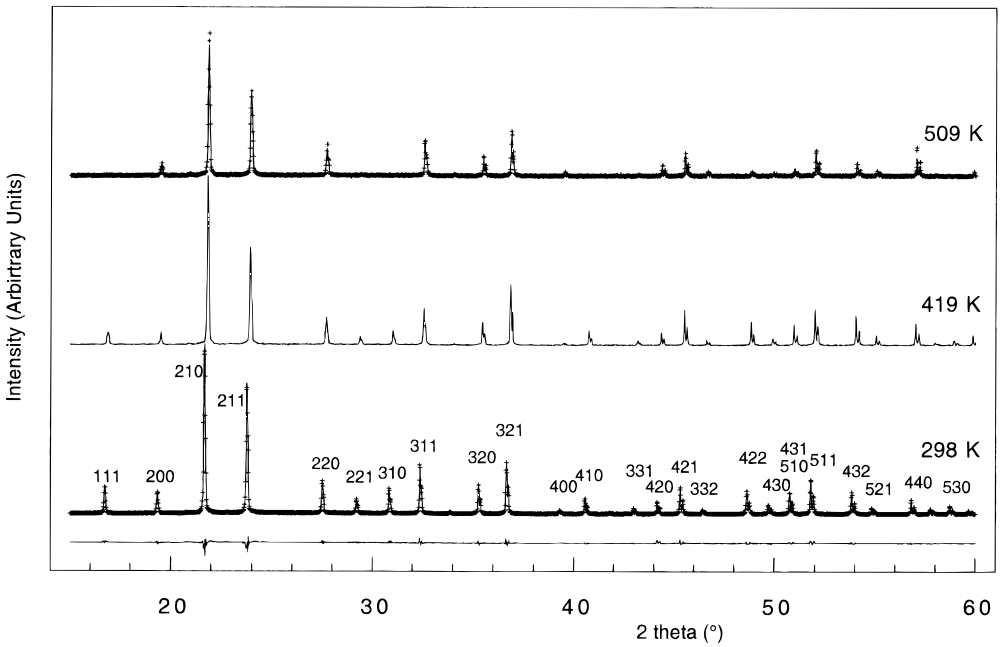

Figure 6. X-ray diffraction patterns at temperatures of 298, 419, and 509 K over a selected 2θ range. At 293 and 509 K, observed (+) and calculated (—) patterns are superimposed. Difference plot for 293 K spectrum shown at bottom of figure. At 419 K, only the observed pattern is shown.

however, evidence of broadening of the bands between 800 and 700 cm^{-1}, which could result from the appearance of a new band at intermediate frequency. Changes in the lattice modes (<300 cm^{-1}) are also observed.

Variable-Temperature Refinements

To gain insight into the structural changes giving rise to the negative thermal expansion of ZrW_2O_8, Rietveld refinement was performed at a total of 14 temperatures between 0.3 and 693 K. Because the overall changes in structure are relatively small, care was taken to ensure a consistent strategy at each temperature. Nonetheless, it should be emphasized that any changes in bond lengths and angles as a function of temperature will always be small relative to their esd's. A cell dimension change of the order of magnitude of that seen experimentally up to the phase transition (9.1823−9.1500 Å), when placed on the same scale as a typical metal−oxygen bond length, represents a change of only 2.000−1.993 Å. This can be compared to a typical Rietveld esd on a bond length of 0.005 Å [the true error is probably larger than this]. It is therefore crucial to adopt a consistent strategy for both data collection and refinement protocol at each temperature. Even changes in the experimental pattern due to the cryostat/furnace backgrounds at high/low temperatures can potentially lead to systematic variations in bond distances/angles of an order of magnitude similar to those under investigation.

Refinements were performed using a number of different methods of treating atomic motion and thermal parameters [isotropic thermal parameters, anisotropic thermal parameters, and rigid-body TLS refinement]. Since we have no evidence to suggest static disorder in this material, we choose to retain the term thermal parameters rather than the perhaps more correct "atomic displacement factor." Regardless of the model used, good agreement to experimental profiles could be achieved at 373 K and below using the low-temperature structure. At 473 K and above, good agreement could be achieved using the high-temperature model. Refinement results for the various models discussed in the text are reported in Table 1. We note that for the high-temperature data sets χ^2 values lower than 1.0 are reported. It is thus questionable whether the number of observations can justify full anisotropic refinement. We emphasize, however, that similarly low χ^2 values are obtained even for the rigid-body model of refinement (vide infra) where only nine atomic variables are refined [e.g., at 693 K, isotropic model: $wR_p = 7.35\%$, $R(F^2) = 16.3\%$, $\chi^2 = 1.0$, 11 parameters; anisotropic model: $wR_p = 5.51\%$, $R(F^2) = 7.01\%$, $\chi^2 = 0.6$, 19 parameters; rigid-body model: $wR_p = 6.0\%$, $R(F^2) = 10.7\%$, $\chi^2 = 0.7$, 9 parameters]. We believe the low χ^2 values to be an artifact of the relatively high furnace background; successful "fitting" of the background resulting in low R factors.[56] It can be seen from Table 1 that there is some nonsystematic variation in wRp values below room temperature. It is possible that minor distortions from cubic symmetry exist at low temperature. Any such distortions are, however, too small to be observed at the resolution of the experimental data [fwhm ca. 0.16° at $2\theta = 120°$].

Isotropic refinement led to an overall average wR_p of 11.77% at room temperature and below and 7.41% above room temperature. The use of anisotropic thermal parameters led to little improvement in agreement factors at room temperature and below, average $wR_p = 11.53\%$, and at the lowest temperature some temperature factors were insignificantly nonpositive definite. Above room temperature a more marked improvement was observed, $wR_p = 6.14\%$ [33 parameters/phase below transition; 19 parameters above transition, W1 and W2 isotropic]. The only major difference noted for the two models of refinement lay in the W2−O3 bond distance between 293 and 373 K. Values for isotropic/anisotropic

(56) Jansen, E.; Schäfer, W.; Will, G. *J. Appl. Crystallogr.* **1994**, *27*, 492−496.

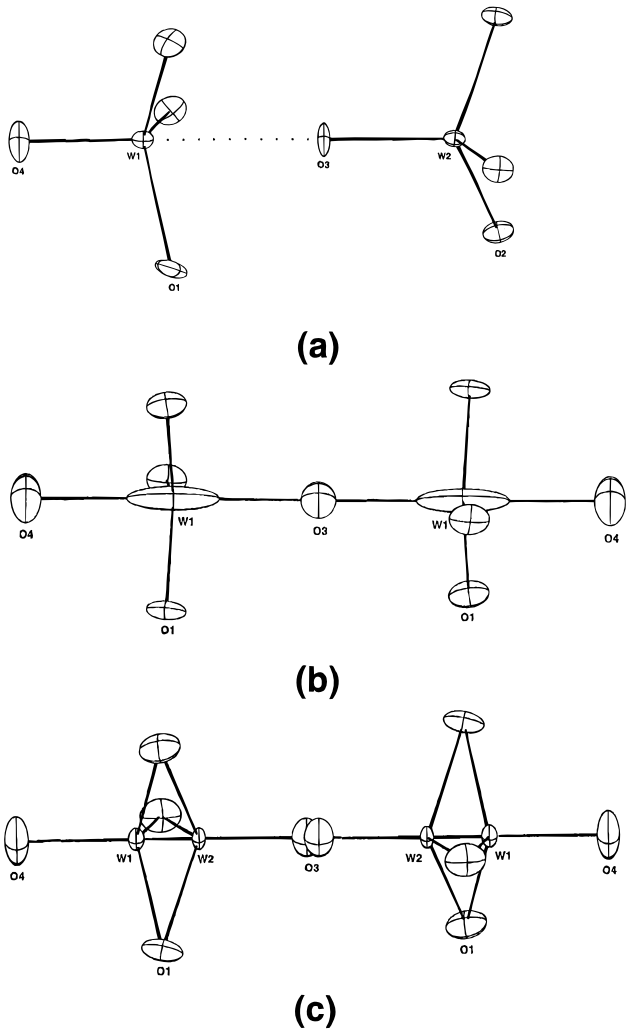

Figure 7. Schematic representation of the WO_4 groups above and below the phase transition. (a) 293 K structure drawn with 90% thermal ellipsoids; (b) refinement at 483 K using a single W site; (c) anisotropic refinement using a split W site, with W1 and W2 thermal parameters allowed to refine freely. For variable temperature refinements, thermal parameters on these two sites were equated.

models at 293, 333, and 373 K are 1.694/1.732, 1.699/1.754, and 1.684/1.721 Å, respectively. Other W−O distances showed an average discrepancy of 0.007 Å (cf. a typical esd of 0.005 Å). These discrepancies are perhaps suggestive of incipient disorder in O3 and W positions as the phase transition is approached.

Figure 10 shows the temperature dependence of selected bond distances and angles within the structure using the anisotropic model both below and above the phase transition. Identical trends are seen using isotropic thermal parameters. It can be seen that there is an apparent decrease in the average M−O bond distance as the temperature is increased. For Zr−O, linear regression yields $d_{av}(Zr-O) = 2.0794-(2.281 \times 10^{-5}T)$ Å. It is well established, however, that the presence of correlated thermal motion in a solid can lead to an apparent reduction in bond length as a function of temperature.[57−59] Such an effect is illustrated schematically in Figure 11. An approximate correction to bond distances for correlated vibrations of rigid bodies is given by[60]

$$R^2_{corr} = R^2_{obs} + 3[u_{eq}(O) - u_{eq}(M)]$$

The application of such a correction to the observed bond distances of Figure 10 gives an overall bond length of $d_{av}(Zr-O) = 2.0794 + (2.67 \times 10^{-6}T)$ Å. This corresponds to a change from 2.0794 to 2.0812 Å ($\Delta d = +0.002$ Å) over the entire temperature range, suggesting that any overall changes in metal−oxygen bond lengths are certainly less than 1 esd.

Examination of the internal bond angles of the constituent polyhedra also reveals no significant changes from 0.3 to 293 K. Between 293 K and the phase transition minor changes in internal polyhedral bond angles and bridging Zr−O−W bond angles are seen. These can presumably be related to anharmonic thermal vibrations as the low−high temperature phase transition is approached. These effects are discussed in more detail below. Because these distortions are observed over only a small temperature range, whereas an essentially linear thermal contraction is observed throughout, it seems unlikely that they are of importance in determining the overall coefficient of thermal expansion.

The observation that minimal distortions of bond distances and angles of the ZrO_6 octahedra occur up to the 428 K phase transition suggests the possibility of modeling the ZrO_6 groups as rigid bodies using the method proposed by Cruickshank[61] and later extended to the translation libration screw model by Schomaker and others.[62−64] In addition, Zr and O thermal parameters showed the expected smooth trends as a function of temperature, with similar values when extrapolated to 0 K, and a more rapid increase with temperature for O than Zr. This model can greatly reduce the number of parameters required to describe thermal motion. The $9n$ parameters required to describe the anisotropic thermal motion of a general n-membered group being replaced by 3 positional, 3 rotational, and a maximum of 20 TLS variables for the entire body.[59]

Rigid octahedra were defined from the 12 K refinement, which showed no significant departures from expected bond distance and angle trends, and for which thermal effects are expected to be low. Above the phase transition, a rigid body based upon the 483 K isotropically refined ZrO_6 group was employed. Using a single diagonal translational and librational term [i.e., $t_{11} = t_{22} = t_{33}$, $l_{11} = l_{22} = l_{33}$; other elements zero] an average wR_p of 11.67% from 0.3 to 293 K was obtained [12 atomic parameters/temperature]. Above 293 K an average wR_p of 6.60% [12 atomic parameters per temperature below, 9 above transition] was obtained. We note that rigid-body refinement causes a reduction in R factor compared to the isotropic model above room temperature from 7.41% to 6.60%, and essentially identical R

(57) Cruickshank, D. W. J. *Acta Crystallogr.* **1956**, *9*, 757.
(58) Busing, W. R.; Levy, H. A. *Acta Crystallogr.* **1964**, *17*, 142−146.
(59) Willis, B. T. M.; Pryor, A. W. *Thermal Vibrations in Crystallography*; Cambridge University Press: Cambridge, 1975.
(60) Downs, R. T.; Gibbs, C. V.; Bartelmehs, K. L.; Boisen, M. B., Jr. *Am. Miner.* **1992**, *77*, 754−175.
(61) Cruickshank, D. W. J. *Acta Crystallogr.* **1956**, *9*, 754.
(62) Pawley, G. S. *Acta Crystallogr.* **1964**, *17*, 457.
(63) Schomaker, V.; Trueblood, K. N. *Acta. Crystallogr.* **1968**, *B24*, 63.
(64) Bartelmehs, K. L.; Downs, R. T.; Gibbs, G. V.; Beiser, M. B., Jr. *Am. Miner.* **1995**, *80*, 680−690.

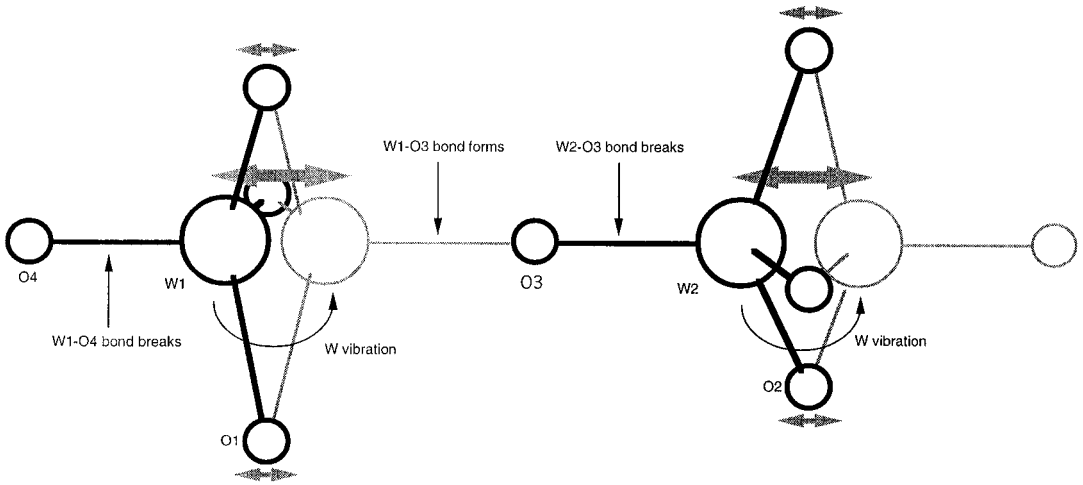

Figure 8. Schematic representation of the inversion of WO_4 groups.

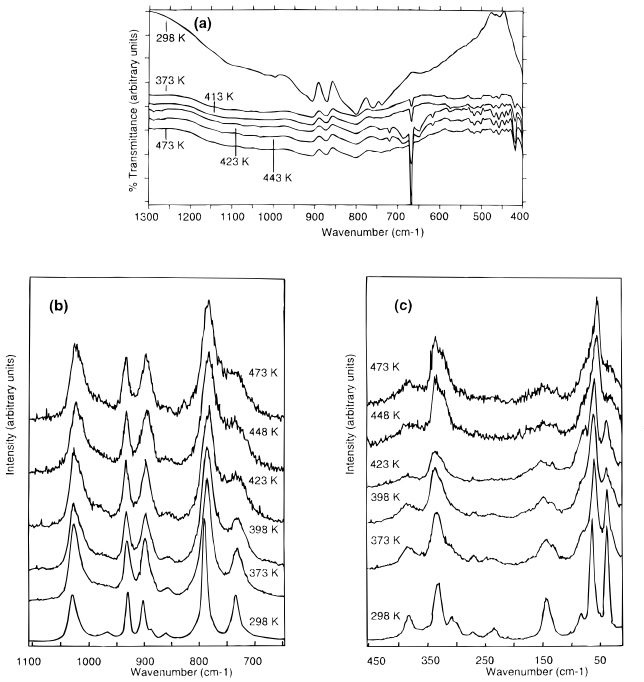

Figure 9. (a) IR and (b), (c) Raman data as a function of temperature.

Table 3. IR and Raman Data at 298 and 473 K[a]

IR (cm^{-1})		Raman (cm^{-1})		
298 K	473 K	298 K	473 K	assignments
		1028_m	1024_m	
999_w		966_w	932_m	$\nu(WO_4)$
907_m	914_w	929_m	896_m	
871_m	873_w	901_m		
		887_w		
800_S	801_w	859_w		
760_m	741_w	789_s	783_s	$\nu_{as}(WO_4)$
739_m	720_w	733_m	739_m	
646_w	688_w			
	668_s			(O−W−O−W−O)
$(600-400)_w$	$(650-450)_{w*}$			
	419_m			(O−W−O−W−O)
		382_w	380_w	$\delta_{as}(WO_4)$
		331_m		$\delta(WO_4)$
		308_w		
		271_w		
		234_w		
		144_m	$148_{b,w}$	lattice modes
		103_w		
		84_w		
		65_m	59_m	
		40_m	$39_{b,w}$	

[a] s = strong; m = medium; w = weak; w* = several weak bands; b = broad.

factors below. This is despite a reduction in the total number of refined atomic parameters from 213 to 147. It is also interesting to compare an *R* factor of 6.60% for the rigid body model above room temperature with that obtained for a free anisotropic model of 6.14%. An improvement in fit of 0.46% is achieved by increasing the number of atomic variables from 63 to 156. Whether or not this improvement in fit is significant considering the increase in parameters is hard to judge. If one assumes the applicability of a standard Hamilton test for these weighted *R* factors,[65] then one would conclude that this improvement is insignificant; i.e., the assumption of a rigid-body model is consistent with the observed data over the entire temperature range.

Refinement of this fully rigid octahedron suggested a small (0.3°) tilt of the ZrO_6 group around the 3-fold axis up to the phase transition. When the polyhedra were allowed to undergo minor distortion, a slight improvement in fit was obtained and this apparent trend was no longer evident. Regardless of the polyhedral model used, however, smooth trends in the librational component of the TLS thermal matrix were obtained. This is discussed in more detail below.

Finally, we note that neutron diffraction data collected close to the phase transition (i.e., at 423 K) showed intermediate behavior. At this temperature the (310) reflection was observed to have decreased markedly in intensity from its value at 293 K, but not to have disappeared completely. As a consequence neither the low- nor the high-temperature model could provide a satisfactory fit to the data. Similar problems have been reported in structure determinations close to the $\alpha-\beta$ transition in quartz.[66] Good agreement could, however, be achieved using a single highly disordered tungsten site. This refinement is reported in Table 1. The gradual nature of the phase transition, as revealed by the gradual changes in the diffraction pattern over a relatively wide temperature range is presumably the

(65) Hamilton, W. C. *Acta Crystallogr.* **1965**, *18*, 502−510.

(66) Heaney, P. J. In *Silica—Physical Behaviour, Geochemistry, and Materials Applications*; Heaney, P. J., Prewitt, C. T., Gibbs, G. V., Eds. *Rev. Miner.* **1994**, *29*, Chapter 1.

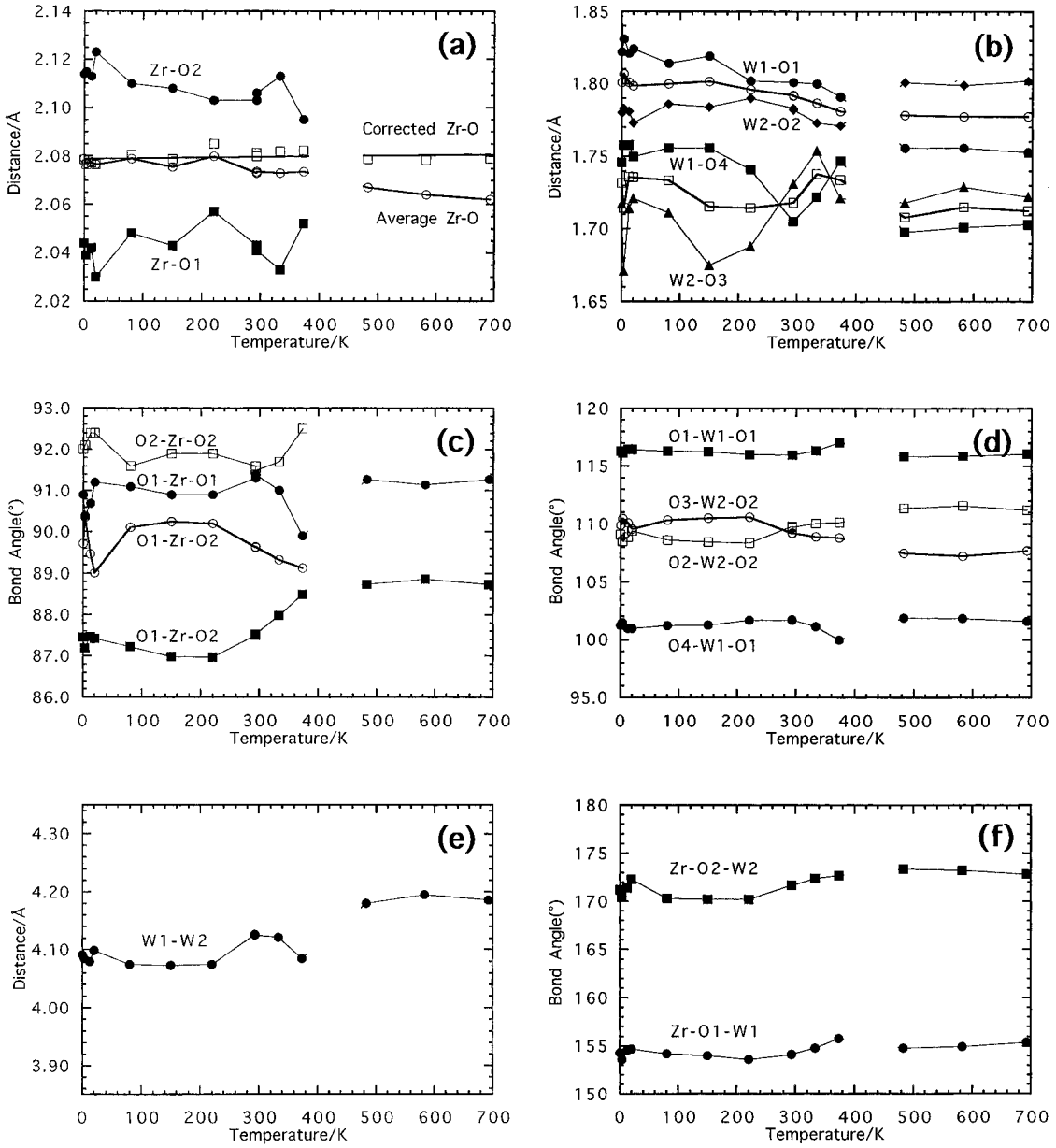

Figure 10. Selected bond distances and angles as a function of temperature. (a) Zr−O bond distances; (b) W−O bond distances (average values of bridging and terminal bonds as open symbols); (c) O−Zr−O bond angles; (d) O−W−O bond angles; (e) W1−W2 distance along 3-fold axis; and (f) Zr−O−W bridging bond angles

reason it was not observed by differential scanning calorimetry.

Discussion of Negative Thermal Expansion

The results discussed above suggest the following conclusions: First, there are no significant changes in metal−oxygen bond distances as a function of temperature which could explain the negative thermal expansion properties of ZrW_2O_8. Second, there are no obvious changes in fractional coordinates as a function of temperature to explain the observed behavior. Third, both ZrW_2O_8 and HfW_2O_8 show the low−high symmetry phase transition at essentially the same temperature and very similar thermal contraction properties. This is in marked contrast to phase transitions in the binaries ZrO_2 and HfO_2.[67] Here the temperature of the monoclinic to tetragonal phase transition differs by around 400 °C. These facts led us to conclude that negative thermal expansion in this material is not due to subtleties of Zr−O, Hf−O, or W−O bonding.[25]

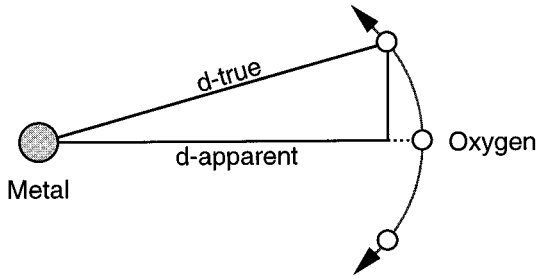

Figure 11. Schematic representation of how correlated thermal motion can lead to an apparent reduction in bond length. Use of a harmonic temperature factor to model the thermally induced rotation of a M−O bond of fixed length will lead to an apparent reduction in M−O bond distances. After Willis and Pryor.[53]

(67) Alper, A. M. *High Temperature Oxides*; Academic Press: New York, 1970; pp 193−216.

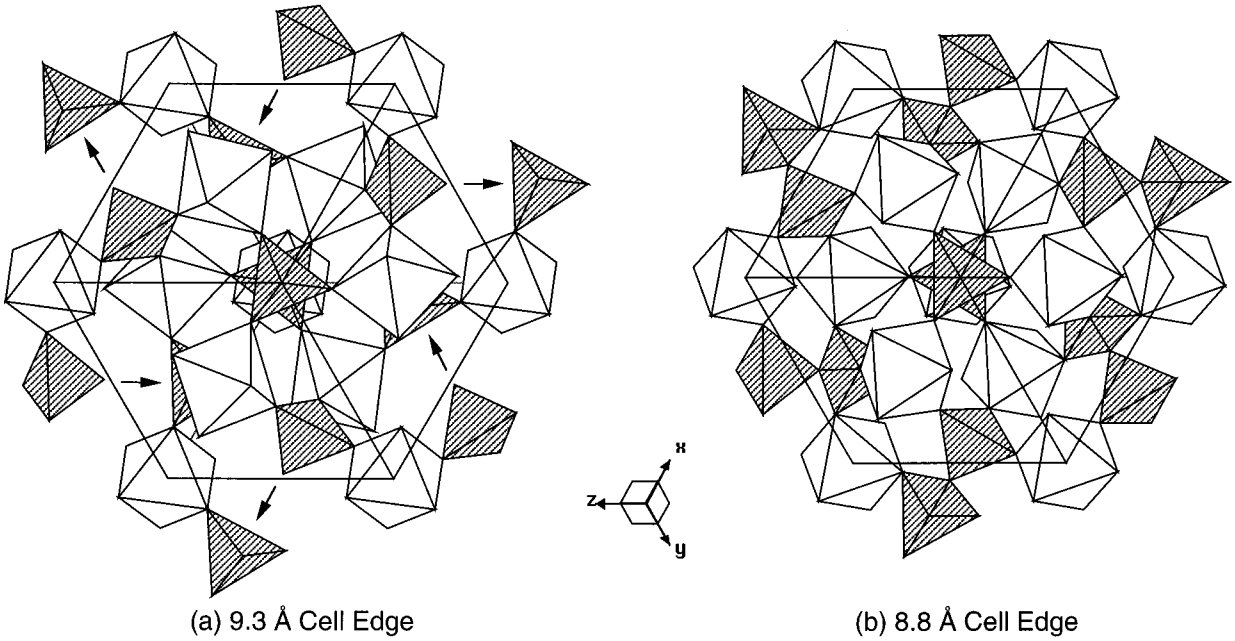

Figure 12. Polyhedral representation of idealized structures down [111] at (a) a cell edge of 9.3 Å and (b) a cell edge of 8.8 Å. The direction of movement of WO_4 tetrahedra (shaded) as ZrO_6 octahedra (unshaded) are tilted is arrowed. Contraction to 8.8 Å brings O3 within bonding range of W1 (see text).

The observation that the magnitude of thermal contraction remains essentially unchanged above and below the phase transition suggests that the negative thermal expansion is an inherent property of this framework topology and is largely independent of the phase transition. We note that to a first approximation the framework structure remains unchanged at the phase transition; in fact, the structure can be usefully viewed as containing corner-sharing ZrO_6 and WO_3 groups, giving a framework stoichiometry of $ZrW_2O_6^{4+}$. The remaining two oxygens can then be introduced in either an ordered (below 428 K, $P2_13$) or a disordered fashion (above 428 K, $Pa\bar{3}$). This picture of the structure is supported by the fact that no significant changes in the ZrO_6 octahedral position is required at the phase transition, which can be thought of as displaying characteristics of both a displacive and reconstructive nature. The oxygens can thus be viewed as becoming "mobile" within a topologically fixed lattice framework. This view is supported by the observed trends in the dielectric data.

We are thus left to conclude that the Zr−O−W bridging oxygen groups are the source of the negative thermal expansion in this material. A systematic change in these angles, corresponding to a coupled twisting of otherwise static polyhedra could give rise to the observed volume changes. Indeed it is well-known that the M−O−M′ potential is considerably shallower for bending distortions than for distortions involving changes in individual M−O bond lengths. Such changes are therefore likely to be energetically facile. The diffraction data do not, however, support a static bending model. This therefore suggests a dynamic model to explain the observed behavior.

Insight into the possible low-energy distortions of this structure (which correspond in a dynamic model to possible low-energy vibrational modes) can be obtained by considering the lattice topology alone. If one makes the assumption that metal−oxygen distances remain unchanged as polyhedra are tilted, then one can investigate potential distortions using distance-least-squares

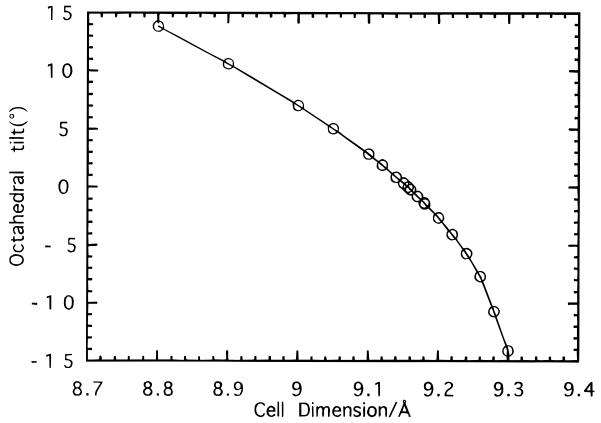

Figure 13. Tilt angle of ZrO_6 octahedra as a function of cell dimension.

procedures. Figures 12 and 13 show the changes in structure imposed as the unit-cell edge is changed. This would correspond to an change in pressure at a constant temperature. Structural changes were modeled by constraining octahedral and tetrahedral angles to their ideal values and bond distances to $d(Zr-O) = 2.108$, $d(W-O_{bridging}) = 1.819$, $d(W-O_{terminal}) = 1.705$ Å. We emphasize that this represents an idealized structure. In particular W1 is restrained to a tetrahedral geometry. As discussed above, the experimental bond angles are significantly distorted (102°/116°) due to the presence of O3.

Using this protocol it is apparent that the connectivity of this lattice gives the structure a remarkable degree of flexibility. Indeed this connectivity can support a cell-edge reduction from 9.3 to 8.8 Å with no distortion of internal polyhedral bond distances and angles. This flexibility is achieved by a rotation of rigid ZrO_6 octahedra around the [111] axis. The coupling of this rotation (via assumed flexible Zr−O−W linkages) results in a marked contraction of the W1−O3 "nonbonded" distance. Figure 13 shows how the polyhedral tilt angle (arbitrarily defined as zero for a cell edge of

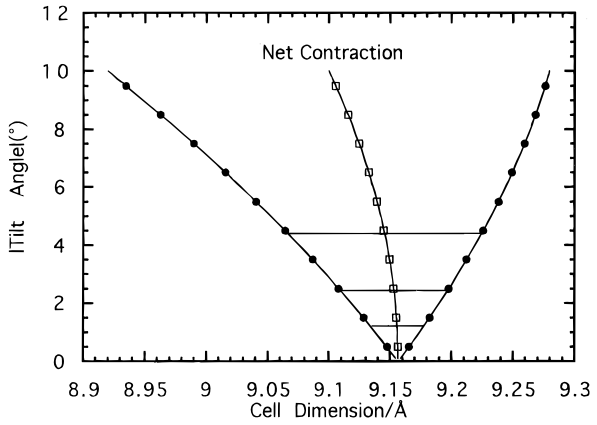

Figure 14. Magnitude of polyhedral tilt vs cell dimension. The net cell parameter as a function of polyhedral tilt is shown. The figure shows how the harmonic libration of ZrO_6 octahedra gives rise to an overall contraction in cell dimension.

9.157 Å; a negative tilt angle corresponds to an anticlockwise rotation when viewed down [111]) depends on the cell edge. Figure 12 shows a view down the [111] axis of the expanded (9.3 Å, low temperature) and contracted (8.8 Å, high temperature) forms of this idealized structure. Clearly, as one continues to contract the structure, the W1−O3 separation will reach a point where it can no longer be considered "nonbonding." Indeed, by a cell edge of 8.8 Å, this distance is reduced to a chemically unreasonable 1.46 Å. This suggests one possible model for the phase transition, which will be discussed in more detail below.

The above discussion describes how the structure can undergo a facile distortion as the cell volume is changed by some arbitrary external force. One can of course reverse this argument and state that a change in polyhedral tilt will result in a change in cell volume. Tilts of rigid bodies such as these can be envisaged as low-energy vibrational modes of the lattice. From Figure 13 one can see that a rotation giving a positive tilt angle, ϕ, will cause a contraction of the cell; one with a negative tilt a contraction. Such modes can be thought of as having negative and positive Gruneisen parameters, respectively.[68] When viewed down the [111] axis, it is also apparent that the Zr−O−W bond angles are close to 180° in projection and remain so over the entire range of tilt angles. It is therefore reasonable to assume that thermal librations of the ZrO_6 octahedra are likely to be (to a first approximation) harmonic in nature, i.e., anticlockwise and clockwise tilts due to thermal motion will have similar magnitude.

It is apparent from Figure 13 that the gradient of the tilt angle vs cell edge plot is not constant: as the tilt angle changes from positive to negative values the rate of change of cell edge decreases. This implies that a tilt of $+\phi$ degrees would give rise to a reduction in cell parameter of greater magnitude than the corresponding increase in cell parameter due to a tilt of $-\phi$ degrees. These effects are perhaps better understood by replotting Figure 13 as tilt magnitude vs cell dimension, as shown in Figure 14. This figure is related to Figure 13 by reflecting the negative tilt values about the tilt equals 0° line. The curve can now be considered in a fashion similar to a potential energy curve for an oscillator in an asymmetric potential well. As the temperature is raised, the energy of the oscillator is raised, here the magnitude of the octahedral libration angle increases. The overall effect on the cell volume will be the average of the contractive and expansive effects due to the positive and negative tilts. As shown in Figure 14, for a harmonic libration the overall cell dimension will decrease as a function of libration angle. These data can then be replotted to give the cell dimension as a function of libration angle. This is shown in Figure 15, along with experimentally determined root-mean-square tilt angles from the TLS model of Rietveld refinement. Despite the simplicity of the structural model the magnitude of cell edge change as a function of libration angle appears gratifyingly close to that obtained experimentally.

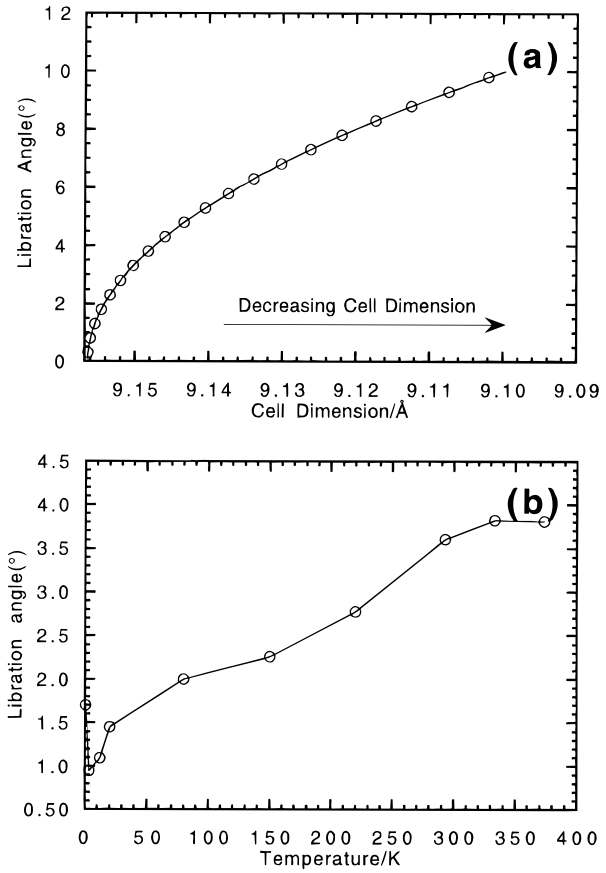

Figure 15. (a) Dependence of overall cell parameter on octahedral libration angle. Note that the cell dimension is plotted on a reverse scale; as libration increases, the cell parameter decreases. (b) Experimentally determined libration angles as a function of temperature from TLS model of refinement.

We emphasize that such a model is supported by the observed structural changes (or lack thereof) in a number of ways. The experimental trends in thermal parameters suggest a significant increase in libration of the rigid ZrO_6 groups as temperature is increased. The lack of any systematic changes in fractional coordinates over the temperature range studied suggests that if thermal vibrations are indeed the cause of negative thermal expansion, they are essentially harmonic in nature. Finally, the reduction in apparent

(68) The Gruneisen parameter, γ_j is defined as d ln ν_j/d ln V, where ν_j is the frequency of the jth normal mode and V the volume. Population of modes with a negative γ_j will give rise to a decrease in the overall volume. The overall Gruneisen parameter, $\nu_{eff} = \sum_j \nu_j \exp(-h\nu_j/kT)/\sum_j \exp(-h\nu_j/kT)$, represents a weighted average over all the populated normal modes, both those with negative (contracting) and positive (expanding) contributions to the overall volume.

average M−O distances for the Zr−O and W−O framework bonds also provides indirect evidence for this model. Each of these framework M−O distances shows a steady and smooth decrease as a function of temperature. This will give rise to a decrease in Zr−W distances and negative thermal expansion, despite there being no significant change in measured Zr−O−W bridging bond angles. We emphasise again, however, that this apparent reduction in bond length does not represent a change in the magnitude of the M−O vector but is an artifact of the increased thermal motion (Figure 11).

The above analogy is related to the rigid unit mode (RUM) analysis proposed by Giddy, Dove, and coworkers and applied with some success to materials such as quartz and the idealized perovskite structure.[69,70] We concentrate, however, on a single low-energy mode of the structure, and one which by definition requires a change in the unit-cell dimensions when active. Thus the vibrational mode considered leads directly to a decrease in unit-cell dimensions. Such a model has the advantage of being readily visualized and can be described in terms of a single easily understood structural parameter: the libration angle ϕ. Our description is thus analogous to the classic treatment of the $\alpha-\beta$ transition in quartz by Megaw.[71] It is important to remember, as emphasized by Megaw, that a description in terms of a single structural parameter will always be an approximation. Provided, however, that the magnitude of change of this single parameter as a function of temperature is significantly greater than other changes, such an approach remains valid. In this specific example we implicitly assume that the mode discussed is of significantly lower frequency (and therefore energy) than other vibrational modes and is therefore most highly populated at each temperature.

Our model can also give some insight into the low−high symmetry phase transition. As a static octahedral tilt becomes larger (more positive), the original "nonbonded" W1−O3 distance decreases markedly and in a linear fashion: $d(\mathrm{W1-O3}) = 2.4286 - 0.07\phi$. Clearly, there will come a point at which this distance becomes too short to be considered nonbonding and O3−O1 repulsive interactions become very large. At $\phi = 10.3°$ the O3-bonded and "nonbonded" distances become equal. As the transition is approached, it seems likely that distortions of the $W1O_4$ tetrahedron will increase and vibrations of constituent atoms will become increasingly anharmonic. The data of Figure 10 support this conclusion. From 293 to 373 K O−W1−O bond angles change from 101.7° to 100.0° and 116.0° to 117.0° (based on anisotropic refinement). At 373 K significant departures can also be seen in Zr−O−W bridging bond angles, and O−Zr−O bond angles. There is also an apparent reduction in W−W separation over this restricted range. As discussed above, however, the positions of W1 and W2 become increasingly ill-defined as the transition is approached and firm conclusions become difficult.

(69) Giddy, A. P.; Dove, M. T.; Pawley, G. S.; Heine, V. *Acta Crystallogr.* **1993**, *A49*, 697−703.
(70) Hammonds, K. D.; Dove, M. T.; Giddy, A. P.; Heine, V. *Am. Miner.* **1994**, *79*, 1207−1209.
(71) Megaw, H. D. *Crystal Structures: A Working Approach*; W.B. Saunders: Philadephia, 1973; Chapter 15.

Conclusion

ZrW_2O_8 has been shown to display a negative coefficient of thermal expansion over its entire stability range of 0.3−1050 K. The structure has been solved from powder diffraction data and refined at various temperatures to gain insight into its unusual properties. The negative thermal expansion is due to transverse vibrations of Zr−O−W bonds, and a model has been proposed involving coupled librations of the constituent polyhedra. Around 428 K the structure undergoes an unusual low−high symmetry phase transition, which results in significant oxygen mobility. This transition has been investigated by diffraction methods, IR and Raman spectroscopies, and dielectric measurements.

These observations lead us to conclude that the presence of a framework lattice of essentially rigid strong M−O bonds and 2-coordinate bridging oxygens is a prerequisite for negative thermal expansion in this type of material. The harmonic nature of the oscillations and retention of cubic symmetry throughout lead to the isotropic nature of the thermal contraction. These observations have led us to the discovery of negative and zero thermal expansion in other families of framework ceramics.

Supporting Information Available: Tables reporting results of isotropic, anisotropic and TLS models of Rietveld refinement at each temperature, and important bond distances and angles (28 pages). Ordering information is given on any current masthead page.

Acknowledgment. We would like to thank Dr. M. C. Shivaglal for recording the IR and Raman data. This work was supported through DOE and through NSF grant No. DMR-9308530.

CM9602959